Developmental Testbed Center Visitor Program Final Report: Development and Application of 3-Dimensional Object Algorithms to High Resolution Forecasts

Adam J. Clark

Cooperative Institute for Mesoscale Meteorological Studies/National Severe Storms Laboratory

1. Introduction

This project utilized a beta version of the Method for Object-based Diagnostic Evaluation Time-Domain (MODE-TD), which, in addition to the spatial dimension, includes the time dimension for object identification. Incorporating time results in a much more powerful diagnostic tool that provides important information to forecasters and model developers on aspects of phenomena like timing, evolution, and translation speed, which would not be available considering the spatial dimension alone. In this project, MODE-TD was applied to 30 h precipitation forecasts from four 4-km grid-spacing members of the 2010 Storm-Scale Ensemble Forecast system run by the Center for Analysis and Prediction of Storms in support of the 2010 NOAA/Hazardous Weather Testbed Spring Forecasting Experiment (Clark et al. 2012). These members used the Weather Research and Forecasting Model and were identically configured except for their microphysics parameterizations, which included the Thompson, Morrison, WSM6, and WDM6 schemes. The main goals include demonstrating new and insightful methods for comparing various aspects of the forecasts and observations that would not be possible without incorporating the time dimension in object identification. Specific characteristics of time-domain objects examined include spatial distribution, duration characteristics, frequency of initiation/dissipation, and translation. Comparisons of average forecast and observed time-domain object attributes are emphasized without attempting to match objects from forecasts to observations.

Most of the data processing and running of MODE-TD on the datasets of interest was accomplished during one month long visit to DTC in July 2012. Further analysis of results and write-up of the results were accomplished at the PI's home institution. Overall, the DTC Visitor Program was a very positive, productive, and rewarding experience. This was made possible through working closely with my host, Tara Jensen, as well as Randy Bullock and other support staff. Tara and Randy made sufficient contributions so that they have been included as co-authors on an article summarizing this work, which will be submitted to the AMS journal *Weather and Forecasting*.

2. Methodology

The WRF simulations were initialized at 0000 UTC and integrated 30 h over a CONUS domain (Fig. 1) with 4-km grid spacing using the Advanced Research WRF model version 3.1.1. Initial and lateral boundary conditions (3 h updates) were from North American Mesoscale model analyses and forecasts, respectively. Forecasts from all four members were available for 35 dates during Spring 2010: 28-30 April; 3-6, 10-14, 17-21, 24-25, 27-28 May; 1-4, 7-11, 14-18 June. Radar data and other high-resolution observations were assimilated into the ICs using a 3DVAR data and cloud analysis system.

Physics parameterizations included the MYJ boundary layer scheme, NOAH land surface model, and Goddard short-wave and RRTM long-wave radiation schemes. As previously noted, the four members differed only by their microphysics parameterizations, which included Thompson,

WSM6, WDM6, and Morrison.

We chose the varied-microphysics members for MODE-TD analyses because there were a reasonable number of members to allow for thorough but not overwhelming statistical analysis of time-domain object attributes. Furthermore, there is a strong scientific interest in examining different microphysics parameterizations in high-resolution models, especially the two "double moment" schemes, WDM6 and Morrison, which were newly available in WRF version 3.1.1.

MODE-TD was applied to 1 h forecast and observed precipitation fields using smoothing radii of 8-, 16, and 32-km and precipitation thresholds of 0.10- and 0.25-inches yielding six unique combinations of parameters. Additionally, objects were required to contain at least 10 grid-points. Finally, the entire area of each forecast and observed time-domain object "bounding-box" was required to fall within the mask pictured in Figure 1. The bounding-box of an object is the rectangular area created using the furthest west and south point within the object as the lower-left corner and the furthest north and east point as the upper-right corner.
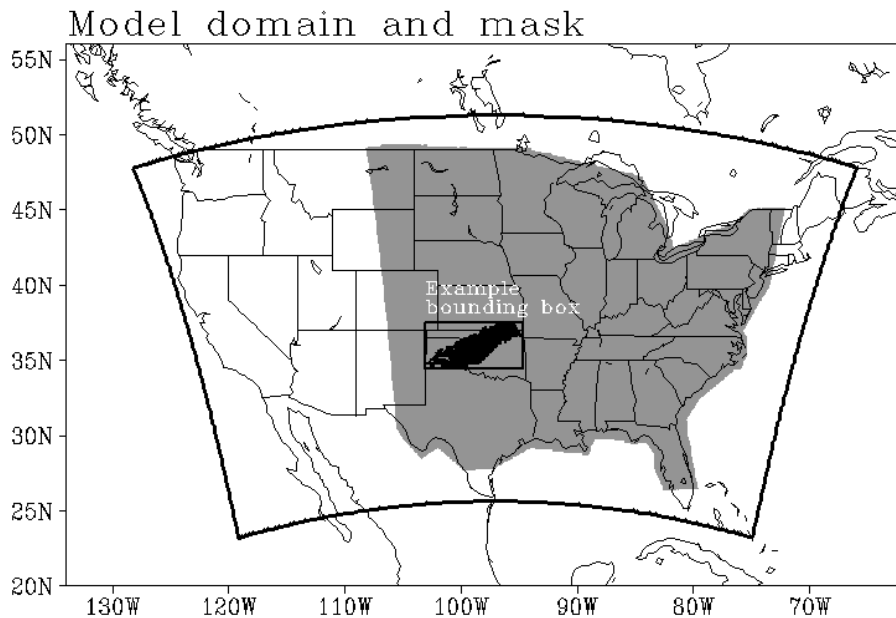

Figure 1 WRF model domain (black outline) and mask (gray shading) within which forecast and observed time-domain objects were analyzed. The black shaded area within the grey mask is the area covered by an example time-domain object along with its corresponding bounding box.

For each time-domain object identified by MODE-TD, 69 attributes were computed (i, j, and t refer to east-west, north-south, and time model grid-coordinates, respectively): (1) object volume (total number of grid-points within an object), (2) − (4) i, j, and t centroid coordinates, respectively, (5) minimum i, (6) maximum i, (7) minimum j, (8) maximum j, (9) minimum t, (10) maximum t, (11) ratio of object volume to bounding box volume, where the bounding box is defined using the maximum/minimum i, j, and t coordinates, (12) u velocity component at forecast hour 2 [i.e., (i-centroid$_{t=2}$ − i-centroid$_{t=1}$)/1 h], (13) v velocity component at forecast hour 2 [i.e., (j-centroid$_{t=2}$ − j-centroid$_{t=1}$)/1 h], (14) u velocity component at forecast hour 3 [i.e., (i-centroid$_{t=3}$ − i-centroid$_{t=2}$)/1 h], (15) v velocity component at forecast hour 3 [i.e., (j-centroid$_{t=3}$ − j-centroid$_{t=2}$)/1 h], …. (68) u velocity component at forecast hour 30 [i.e., (i-centroid$_{t=30}$ − i-centroid$_{t=29}$)/1 h], (69) v velocity component at forecast hour 30 [i.e., (j-centroid$_{t=30}$ − j-centroid$_{t=29}$)/1 h]. For the first hour an object was present and when the object did not exist, missing values of -9999.0 were assigned to the u and v velocity components. Centroid coordinates were computed using the mean i, j, and t over the object volume.

3. Results

a) Spatial distribution of time-domain objects

Locations of precipitation object tracks defined using the 0.10-in precipitation threshold over the entire 35 day analysis period are shown by lines connecting object centroids at their first and last time for Thompson and Stage IV observations in Figure 2, and corresponding object track frequencies within 0.5 x 0.5 degree lat/lon grid-boxes are shown in Figure 3.
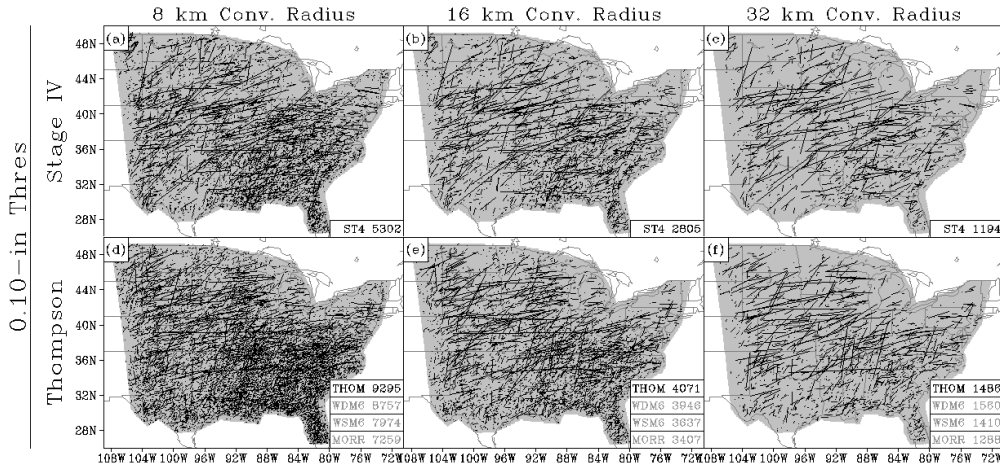

Figure 2 Lines connecting start- and end-points of time-domain precipitation objects identified in the Stage IV data using the 0.10-in rainfall threshold and smoothing radii of (a) 8-km, (b) 16-km, and (c) 32-km. (d) – (f) same as (a) – (c) except for the set of simulations using the Thompson microphysics scheme.
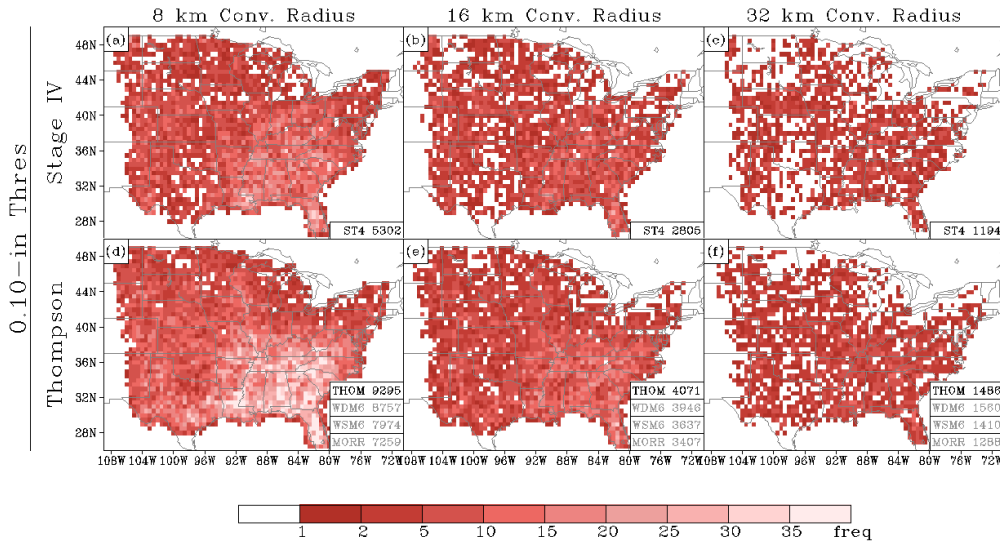

Figure 3 Same as Figure 2, except each panel shows the number of "tracks" as shown in Fig. 2 that intercepted 0.5 x 0.5 degree grid-boxes.

The non-Thompson schemes are not shown to simplify the plots, but their spatial distributions of object tracks were very similar to those of Thompson. In the simulations and observations, the total number of tracks (indicated at bottom left of each Fig. 2 and 3 panel) decreases with increasing smoothing radius. This reduction is consistent with smoothing reducing the precipitation amplitude so that fewer areas reach the criteria for object classification. Additionally, smoothing can cause closely

3

separated areas of precipitation to combine into one, further reducing object numbers. On the other hand, in certain cases smoothing could increase the number of objects. For example, consider one object comprised of two areas of relatively heavy precipitation separated by light/moderate precipitation. If smoothing damps the amplitude of the light/moderate precipitation enough so that it falls below the threshold required for object classification, the two areas of heavy precipitation would no longer be "connected" and would thus comprise two separate time-domain objects.

The different smoothing radii also impact the spatial distribution of object tracks. For the smallest radius, there is a clear maximum in object frequencies over the southeast US. However, as the smoothing radius increases, the southeast US maximum disappears and the spatial distribution of objects becomes quite uniform. The reduction over the southeast US implies that, although precipitation may be more frequent, objects here tend to be smaller, shorter-lived, and less intense than those over other regions and thus more easily filtered out by a large smoothing radius.

At all thresholds and smoothing radii (including those not shown), all four microphysics parameterizations over-predict the total number of time-domain objects. This result is not surprising as the tendency for convection-allowing models to over-predict precipitation is well documented. Generally, Thompson over-predicts the most, while Morrison over-predicts the least.

b) Object duration statistics

Object number as a function of duration for the 0.10-in precipitation threshold is shown in Figures 4. To eliminate the impact of over-prediction on the shape of the distributions, the object numbers for each duration were normalized by the total number of objects for each threshold/radius (Figs. 4d-f). For the 0.10-in rainfall threshold and the 8-km smoothing radius (Fig. 4a), the number of objects in the models and observations peak at 3 h duration and then quickly tail off for longer durations. The over-prediction of object numbers is apparent as well, with the peak at 3 h in the Thompson and WDM-6 schemes almost twice that of Stage IV observations. However, considering the normalized object frequencies, all the simulations replicate the shape of the observed distribution quite well (Fig. 4d). The models do not depict the distribution of object durations as well for higher rainfall thresholds (not shown).
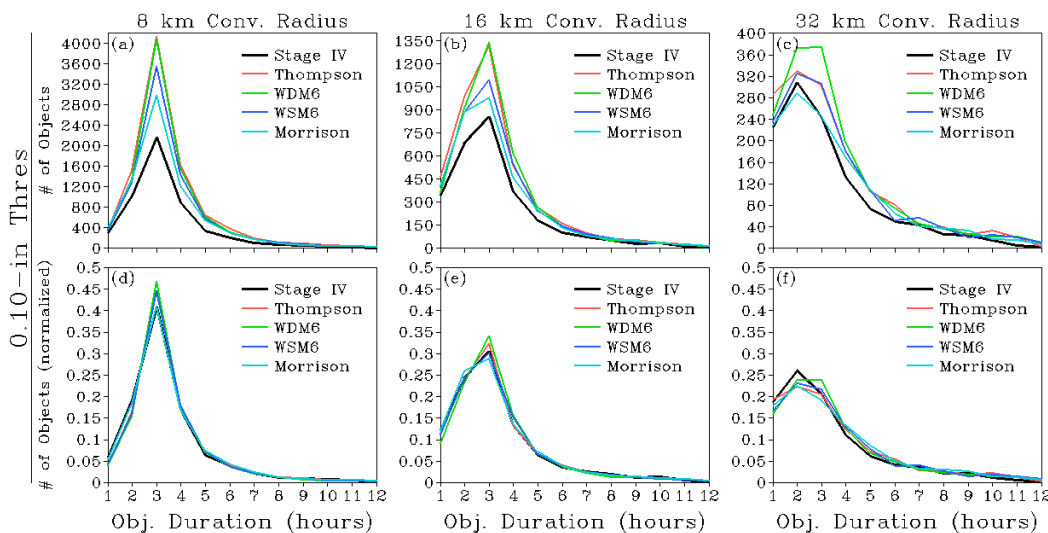

Figure 4 The number of time-domain precipitation objects as a function of duration (hours) in forecasts and corresponding observations using the 0.10-in rainfall threshold and smoothing radii of (a) 8-km, (b) 16-km, and (c) 32-km. (d) – (f) same as (a) – (c) except the number of objects at each duration for each dataset is normalized by the total number of objects across all durations in each dataset.

d) Diurnal cycle of object frequencies

The total number of objects present at each forecast hour identified using the 0.10-in threshold and 8-km smoothing radius is shown in Figs. 5a-d. Because MODE-TD provides object start and end time, objects at each forecast hour can be separated according to the hour at which they initiated. Thus, at each hour in Figs. 5a-d, the height of individual segments comprising each histogram bar indicate the number of objects initiating at a specific forecast hour, with the color of the segments indicating the hour the objects originated. For example, at forecast hour 21 in Figs. 5a-d, the top segment colored dark red indicates the number of observed objects that initiated at that hour. The white segment immediately below indicates the number of observed objects that initiated the previous hour (forecast hour 20) and still present at hour 21. The light pink segment below the white segment indicates objects initiating 2 h before (i.e., forecast hour 19) and still present at hour 21, and so on. The segments are stacked so that forecast hour 1 is always at the bottom, which allows one to follow segments with a particular color forward in time to see how quickly objects initiating from a particular hour dissipate.
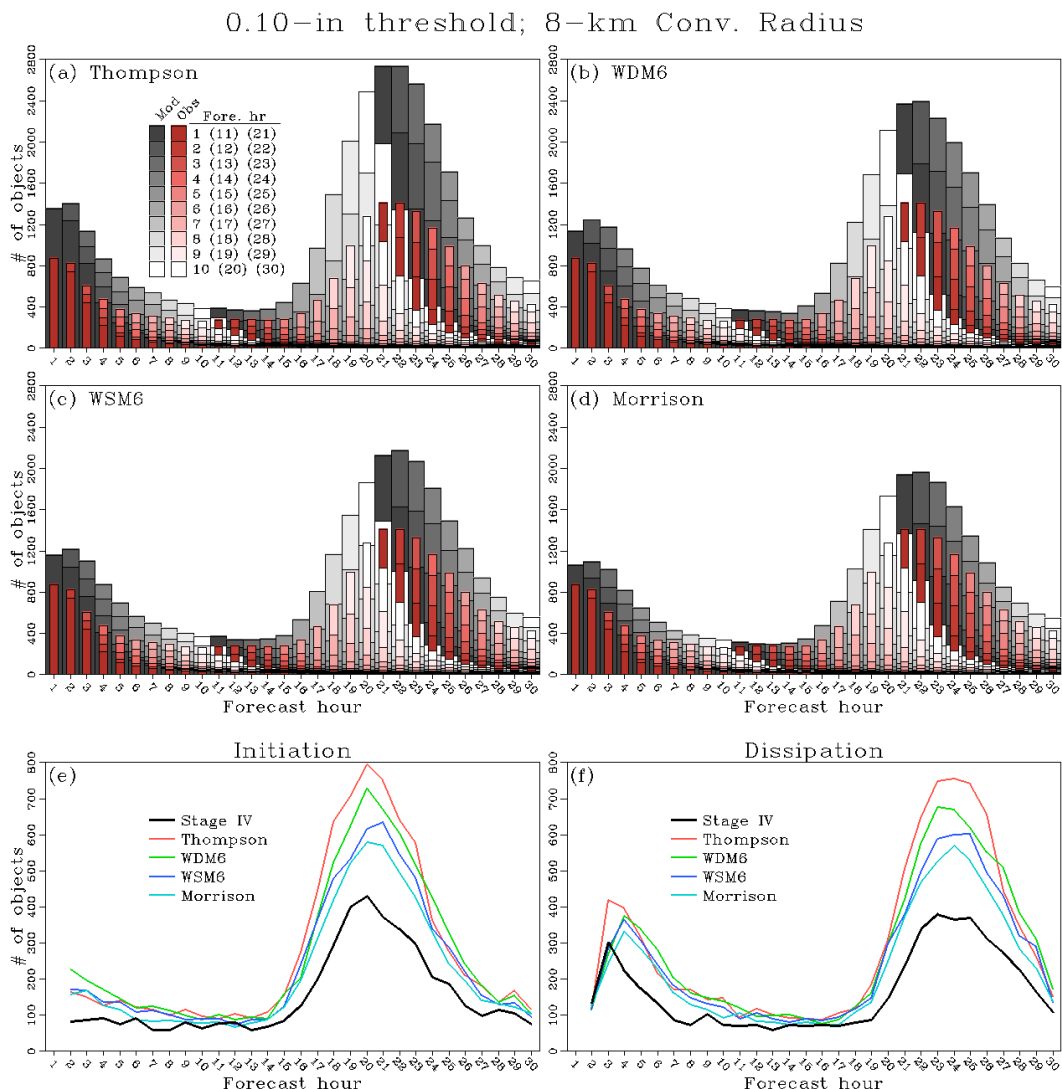

Figure 5 The height of the stacked histogram bars indicates the total number of time-domain precipitation objects at each forecast hour identified using the 0.10-in rainfall threshold and 8-km smoothing radius for (a) Thompson, (b) WDM-6, (c) WSM-6, and (d) Morrison. In each of the (a) – (d) panels, histogram bars for the Stage IV objects are shaded pink/red and overlaid on those of the model, which are shaded black/white. For each forecast hour, the height of the individual segments comprising each "stack" indicate the number of objects originating during the forecast hour indicated by the color of the segment. The segments on top always indicate the number of objects that initiated at the marked forecast hour and those on the bottom are always for forecast hour 1. A legend for the colored histogram bars is provided in panel (a). The number of objects that (e) initiated and (f) dissipated at each forecast hour (explained further in text).

5

Generally, for the 0.10-in rainfall threshold and 8-km smoothing radius, the simulations depict the shape of the diurnal cycle in object frequencies quite well, with a gradual decrease from a relative peak at the initial hour to a relative minimum between forecast hours 9 and 14, followed by a sharp increase to a peak at forecast hours 21 and 22. However, consistent with previous results, the simulations over-predict object frequencies quite uniformly across all hours, with Thompson over-predicting the most and Morrison the least, which is most apparent comparing the magnitude of the forecast hour 21-22 peak.

The frequency of object initiation and dissipation can also be computed and is shown in Figures 5e and f, respectively. Consideration of initiating/dissipating object frequencies is important because they control the rate of change in the object numbers at a particular forecast hour [i.e. more (less) initiating relative to dissipating objects results in an increase (decrease) in total objects]. The number of initiating objects is simply defined as the number of objects with their first time at a given forecast hour. In Figs. 5a-d, the number of initiating objects at each hour is indicated by the height of the top bar in each set of stacked histograms. The number of dissipating objects at a particular forecast hour is defined as the number of objects from the previous hour no longer present.

For the Stage IV observations, the number of initiating objects remains nearly constant between forecast hours 2 through 15, begins increasing at forecast hour 16, reaches a peak at forecast hour 20, and then decreases until flattening again at about forecast hour 27 (Fig. 5e). The peak in initiating objects lags the peak in total objects by about 1 to 2 h because the number of dissipating objects remains less than initiating ones until about forecast hour 22. In the simulations, the shape of the diurnal cycle in initiating objects is similar to that of the Stage IV observations, however, instead of a relatively constant number of initiating objects between forecast hours 2 and 15, there is a gradual decrease in the simulations. Additionally, although the peak in initiating objects in the simulations occurs at about the same time as Stage IV observations, the amplitude of the peak is too high in the simulations.

The pattern in the diurnal cycle of dissipating objects for the simulations and Stage IV observations (Fig. 5f) generally follows that of initiating objects, except there is a small maximum in dissipating objects near the beginning of the forecast period and the maximum near forecast hour 24 lags that of initiating objects by about 3 to 4 hours. The 3 to 4 hour lag between initiating and dissipating object frequencies is consistent with the peak in observed and simulated object lifetimes at the 0.10-in threshold and 8-km smoothing radius of 3 h (Fig. 5a).

The diurnal cycle of object frequencies for other rainfall thresholds and smoothing radii will be shown in the version submitted to a journal.

e) Time-domain object velocities

The *u* and *v* components as well as total speed (magnitude) of objects are shown as a function of forecast hour in Figure 6. At each hour, average velocity components are computed over all the objects that were present and had valid velocity components. Additionally, at each hour, the distribution of velocities in each of the simulations was compared to that of the observations to determine whether the difference in means was statistically significant at level $\alpha = 0.05$. For the significance test, a Welch two-sample t-test was employed using the *t.test* function in the R statistical software package. The presence of colored bars along the x-axis in each Figure 6 panel, where the specific colors correspond to the particular microphysics scheme, indicates that differences in the mean velocity component of the simulation was significantly different than that of the Stage IV observations.

For the average *u* velocity components, there is a clear diurnal cycle in both the simulations and observations with a broad peak centered near forecast hour 12 and a broad minimum around forecast hours 21-23. We believe this diurnal cycle is related to the large peak in initiating objects around forecast hour 21. At this time, which corresponds to maximum insolation, "air-mass" thunderstorms

commonly occur in moist environments with weak upper-level flow that results in slow movement. Rainfall systems existing at other times within the diurnal cycle are more likely to be associated with a synoptic scale weather system and/or be driven by mesoscale processes that require stronger vertical wind sheer, and thus, these types of systems would have faster speeds than the rainfall systems tied to solar heating.

Generally, average *u* components in the simulations are slower than in observations. The differences are particularly large during the first 6 to 9 hours of the forecasts when the simulations are too slow by anywhere from 4 to 8 km/h, depending on which microphysics scheme, rainfall threshold, and smoothing radius is considered. This slow bias during the first part of the forecast has been documented for convection-allowing simulations that do not use radar data assimilation. However, for simulations that use the radar-data-assimilating 3DVAR system like those examined herein, only anecdotal evidence of a slow bias during the first few forecast hours has been documented during annual SFEs. The slow bias likely at least partially results from the 3DVAR system not adequately depicting the mesoscale dynamics/circulations driving the movement of convective systems existing at the model initialization time. We have observed through model evaluations conducted for the annual SFEs that even when convection is well depicted in the initial conditions of these simulations, there is often a period of time during the first hour or two of model integration when storms lose their coherency but then "spin-up" again as the model dynamics begin to take control. This spin-up is likely reflected in the slow bias seen here.
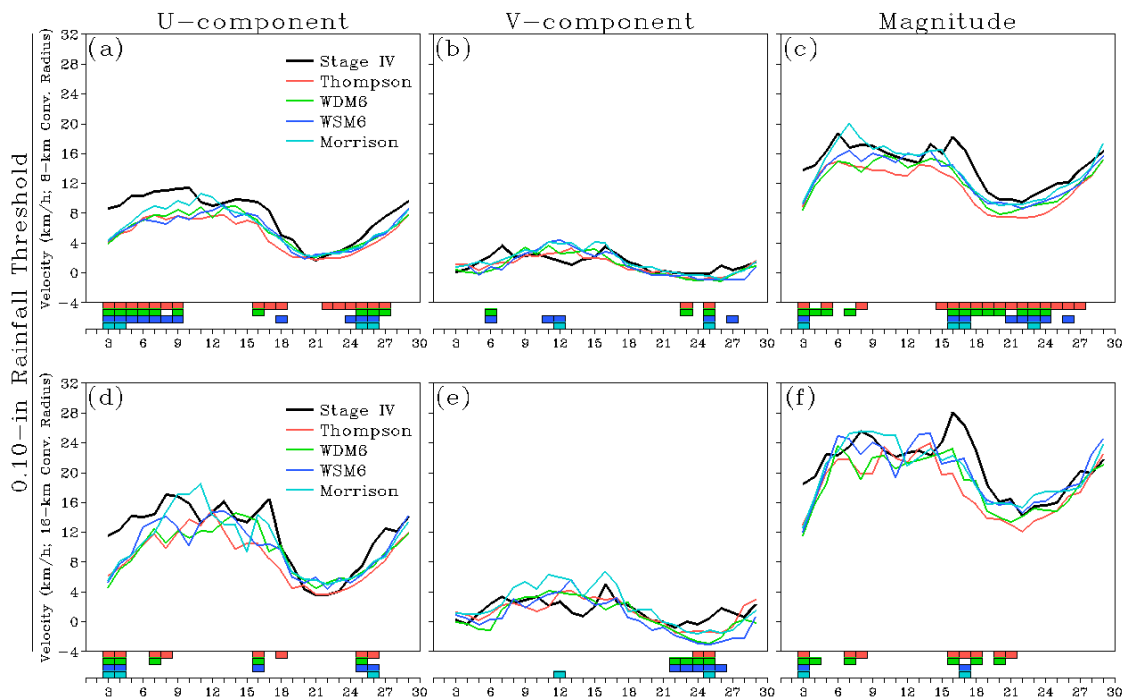

Figure 6 Average velocity components at each forecast hour for time-domain objects in observations and simulations defined using the 0.10-in rainfall threshold and 8-km smoothing radius: (a) u-component, (b) v-component, (c) magnitude. (d) – (f) Same as (a) – (c), except for objects defined using a 16-km smoothing radius. A legend is provided in the left-hand-side panels. The colored boxes just above the x-axis in each panel indicate that the differences at the particular hour between the simulation and observations are statistically significant. The colors indicated in the legend also apply to the filled boxes.

The average *v* components (Figs. 6b, e) in the simulations and observations generally fall within the range -4 to 4 km/h, which is much smaller than the average *u* components that vary between about 4 and 20 km/h. Although there are a few times with statistically significant differences between the

various simulations and observations, there do not appear to be any systematic differences with the exception of perhaps forecast hours 21 to 27 when the average *v* velocity components in the simulations are generally smaller than those in the Stage IV observations.

The average velocity magnitudes (Figs. 6c, f) generally follow the same pattern as the *u* components, but with larger values – generally in the range 8 to 30 km/h. Similar to the *u* components, the simulations have a slow bias at most forecast hours. The Thompson scheme, on average, has the largest slow bias, and at each smoothing radius and rainfall threshold considered, Thompson has the most statistically significant differences.

To examine the evolution of the average velocity components over the lifetime of time-domain objects, the average components are presented as a function of object duration in Figure 7. This is equivalent to setting the initiation time of each object to a common hour and then computing the average components at each hour within the object lifetime. Note, because the number of objects decreases sharply with increasing duration, the sample sizes used to compute the averages have a corresponding decrease with increasing duration. Thus, average velocities in the first few hours of object lifetimes are much more heavily weighted to objects with shorter lifetimes. In Fig. 7, the under-laid grey bars indicate the sample size of the time-domain objects in the observations for each of the durations, and the colored bars along the x-axis of each panel show the object durations at which significant differences in average velocities between the simulations and observations were present.
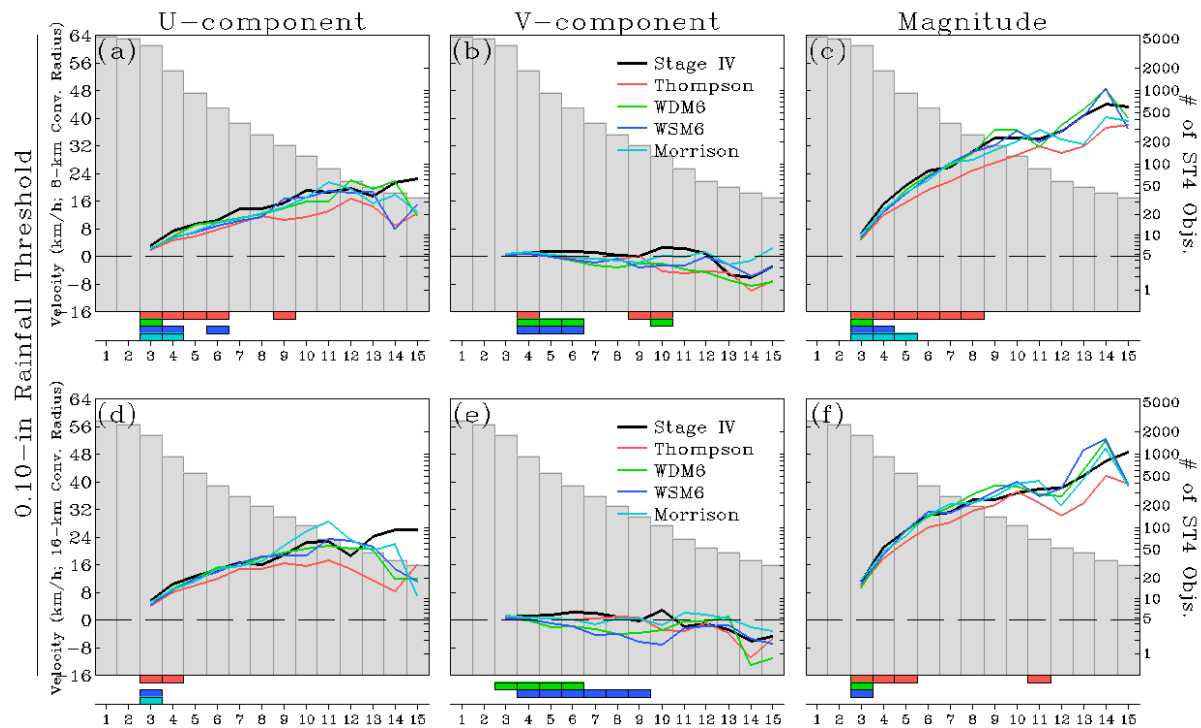

Figure 7 Colored lines indicate average velocity components (km/h) for observations and simulations over the lifetime of time-domain objects. Grey histogram bars indicate the number of Stage IV time-domain objects equal to or exceeding each value of duration. The y-axis for the velocities (number of objects) is on the RHS (LHS) of each panel. The colored boxes just above the x-axis in each panel indicate that the differences at the particular hour between the simulation and observations are statistically significant. The colors indicated in the legend in the middle column panels also apply to the filled boxes. For the 0.10-in rainfall threshold and 8-km smoothing radius (a), (b), and (c) show the u-component, v-component, and magnitudes, respectively. (d) – (f) same as (a) – (c) except for 16-km smoothing radius.

8

For the average *u* components (Figs. 7a, d), there is a clear upward trend in both simulations and observations with increasing object duration. Overall, the average *u* velocities in the simulations are too slow, with the WDM6, WSM6, and Morrison simulations roughly clustered together and the Thompson simulations slower, which is reflected in there being more times at which the average *u* velocities in Thompson are significantly different compared to the observations. The slow bias in all simulations is most pronounced during the first 8 h of object lifetime.

For the average *v* components (Figs. 7b, e), the observations generally stayed near zero indicating that, on average, time-domain objects have no preference for northward or southward movement. In the models, there is a slight tendency for systems to move more southerly with increasing lifetime. In general, the average *v* velocities in the simulations were slightly less (i.e., more southerly) than the observations. In particular, at hours 6-10 for the 0.10-in rainfall threshold/16-km smoothing radius (Fig. 7e), the average *v* velocities in the WSM6 and WDM6 simulations were noticeably less than the observations indicating too much southerly movement.

Despite the aforementioned biases in the individual velocity components, the WSM6, WDM6, and Morrison simulations follow the observed average magnitudes very closely with only a few times near the beginning of the average time-domain object lifetime that differences relative to the observations are significant (Figs. 7e, i). On the other hand, the average Thompson magnitudes are clearly outliers relative to the other runs, exhibiting obvious slow biases of about 6-8 km/h. Thompson also has the most times at which differences relative to the observations are statistically significant. Furthermore, there is acceleration with increasing object lifetime similar to that observed in the average *u* velocities, except the acceleration is even more pronounced. This acceleration could be real, or, if there is a tendency for shorter-lived objects to have slower speeds, it could simply be an artifact of these objects having more weight during the first few hours of the average object's lifetime.

4. Conclusion

The addition of the time dimension in the MODE-TD software allowed for relatively straightforward evaluation of rainfall system attributes that should be very useful to model users and developers. In the future, we believe that MODE-TD concepts will continue to have particularly useful applications to convection-allowing (i.e., 1-4 km grid-spacing) and convection-resolving (i.e., grid-spacing ≤ 1 km) forecast systems, because it will allow for an efficient and objective method to evaluate explicitly-depicted convective phenomena such as supercells, MCSs, and flash-flood producing rainfall systems. This future work will require the use and development of fuzzy-logic-based algorithms to match and/or merge object in the forecast and observed time-domain fields, which was not attempted in this study.

References

Clark, A. J., and Coauthors, 2012a: An overview of the 2010 Hazardous Weather Testbed Experimental Forecast Program Spring Experiment. *Bull. Amer. Meteor. Soc.*, **93**, 55-74.

Reference for manuscript to be submitted based on work presented herein:

Clark, A. J., R. G. Bullock, T. L. Jensen, M. Xue, and F. Kong, 2013: Application of object-based time-domain diagnostics for tracking precipitation systems in convection-allowing models. Wea. Forecasting, (to be submitted).